The Astrophysical Journal, 823:87 (11pp), 2016 June 1 doi:10.3847/0004-637X/823/2/87
© 2016. The American Astronomical Society. All rights reserved.

THE DENSE GAS IN THE LARGEST MOLECULAR COMPLEXES OF THE ANTENNAE: HCN AND HCO^+ OBSERVATIONS OF NGC 4038/39 USING ALMA

Maximilien R. P. Schirm[1], Christine D. Wilson[1], Suzanne C. Madden[2], and Dave L. Clements[3]
[1] Department of Physics and Astronomy, McMaster University, Hamilton, ON L8S 4M1 Canada; schirmmr@mcmaster.ca, wilson@physics.mcmaster.ca
[2] Laboratoire AIM, CEA, Université Paris VII, IRFU/Service d'Astrophysique, Bat. 709, F-91191 Gif-sur-Yvette, France
[3] Astrophysics Group, Imperial College, Blackett Laboratory, Prince Consort Road, London SW7 2AZ, UK
Received 2015 August 11; accepted 2016 April 1; published 2016 May 25

ABSTRACT

We present observations of the dense molecular gas tracers HCN, HNC, and HCO^+ in the $J = 1 - 0$ transition using the Atacama Large Millimeter/submillimeter Array. We supplement our data sets with previous observations of CO $J = 1 - 0$, which trace the total molecular gas content. We separate the Antennae into seven bright regions in which we detect emission from all three molecules, including the nuclei of NGC 4038 and NGC 4039, five super giant molecular complexes in the overlap region, and two additional bright clouds. We find that the ratio of L_{HCN}/L_{CO}, which traces the dense molecular gas fraction, is greater in the two nuclei ($L_{HCN}/L_{CO} \sim 0.07 - 0.08$) than in the overlap region ($L_{HCN}/L_{CO} < 0.05$). We attribute this to an increase in pressure due to the stellar potential within the nuclei; a similar effect to what has been seen previously in the Milky Way and nearby spiral galaxies. Furthermore, the ratio of $L_{HNC}/L_{HCN} \sim 0.3 - 0.4$ does not vary by more than a factor of 1.5 between regions. By comparing our measured ratios to photon dominated region (PDR) models including mechanical heating, we find that the ratio of L_{HNC}/L_{HCN} is consistent with mechanical heating contributing $\gtrsim$5%–10% of the PDR surface heating to the total heating budget. Finally, the ratio of L_{HCN}/L_{HCO+} varies from ~1 in the nucleus of NGC 4038 down to ~0.5 in the overlap region. The lower ratio in the overlap region may be due to an increase in the cosmic ray rate from the increased supernova rate within this region.

Key words: galaxies: individual (NGC 4038, NGC 4039) – galaxies: interactions – galaxies: ISM – ISM: molecules

1. INTRODUCTION

Merging and interacting galaxies play a fundamental role in the hierarchical evolution of galaxies (e.g., Steinmetz & Navarro 2002). In a major merger, the turbulent motion generated by the gravitational interaction between the two merging galaxies can lead to a significant increase in the star-formation rate, usually in the form of starbursts (e.g., see Hopkins et al. 2006 and references therein). For the most extreme mergers, this enhancement can culminate in an ultra luminous infrared galaxy (ULIRG, $L_{IR} > 10^{12}$; Sanders & Mirabel 1996). In fact, it has been shown that most, if not all, ULIRGs are the direct result of an ongoing merger (Sanders et al. 1988; Clements et al. 1996; Sanders & Mirabel 1996).

In the nearby universe, the closest example of a major merger is the Antennae (NGC 4038/39, Arp 244), with the two progenitor galaxies, NGC 4038 and NGC 4039, still in a relatively early merger stage. Within this system, the region where the two initial gas disks are believed to overlap has been dubbed the "overlap region" (Stanford et al. 1990); it has also been referred to as the "interaction region" (Schulz et al. 2007). Young, massive ($>10^6 M_\odot$), compact "super star clusters" (SSCs) are found throughout the overlap region (Whitmore et al. 1999, 2010), which also plays host to five super giant molecular complexes (SGMCs; Wilson et al. 2000), that is, massive ($>10^8 M_\odot$) associations of molecular gas within which current and future star formation is expected.

The molecular gas in the Antennae has been studied predominantly using the molecular gas tracer CO, which is excited via collisions with H_2. The total molecular gas content within the Antennae, assuming a Milky Way-like CO-to-H_2 conversion factor, is $\sim 2 \times 10^{10} M_\odot$ (Gao et al. 2001). Interferometric observations of CO $J = 1 - 0$ show the presence of 100 super giant molecular clouds (SGMCs) throughout the system with a mass range of $\sim 10^7$–$10^9 M_\odot$ (Wilson et al. 2003). More recently, Schirm et al. (2014) analyzed observations of CO $J = 1 - 0$ to $J = 8 - 7$ using a non-local thermodynamic equilibrium (non-LTE) radiative transfer analysis. They found that most of the molecular gas in the system is cool ($T_{kin} \sim 10 - 30$ K) and intermediately dense ($n(H_2) \sim 10^3 - 10^4$ cm^{-3}), while a small fraction (~0.3%) of the molecular gas is in a warm ($T_{kin} \gtrsim 100$ K), dense ($n(H_2) \gtrsim 10^4$ cm^{-3}) phase.

Recently, Herrera et al. (2012) combined high-resolution Atacama Large Millimeter/submillimeter Array (ALMA) science verification observations of CO $J = 3 - 2$ in the Antennae with VLT/SINFONI imaging of the H_2 1 − 0 S(1) transition, while Whitmore et al. (2014) obtained ALMA cycle-0 observations of the overlap region in CO $J = 3 - 2$. By combining their data with observations from the *Hubble Space Telescope* (*HST*) and the Very Large Array (VLA), Whitmore et al. (2014) identify regions within the overlap region corresponding to the various stages of star formation—from diffuse giant molecular clouds (GMCs) all the way to intermediate and old stellar clusters. Of particular interest is the very bright CO $J = 3 - 2$ emission found within SGMC 2, which Whitmore et al. (2014) dubbed the "firecracker" and which is believed to be the precursor to a SSC. In addition, strong H_2 1 − 0 S(1) emission is associated with the bright CO $J = 3 - 2$ emission (Herrera et al. 2012). The mass and energetics of the cloud suggest a very high pressure ($P/k_B \gtrsim 10^8$ K cm^{-3}), while a lack of thermal radio emission indicates that no star formation has yet occurred (Johnson et al. 2015).

While CO is the most commonly used tracer of molecular gas, due to its brightness and relatively high abundance in GMCs, it may not be the ideal tracer for the star-forming

molecular gas. Dense gas tracers, such as HCN (Gao & Solomon 2004a, 2004b; Papadopoulos 2007), HNC (Talbi et al. 1996), and HCO^+ (Graciá-Carpio et al. 2006), can be used to study the molecular gas most directly linked to star formation. This relation culminates in the form of a tight relationship between the luminosity of HCN (L_{HCN}) and the infrared (IR) luminosity (L_{IR}), which is tighter than the correlation between CO and the infrared luminosity (Liu & Gao 2010). In fact, this relationship holds in the form of a constant ratio of L_{HCN}/L_{IR} from individual GMCs all the way up to luminous infrared galaxies (LIRGs; Wu et al. 2005b). Recently, Bigiel et al. (2015) used CARMA data to compare HCN and other dense tracers to the far-infrared luminosity to trace star-formation efficiency and dense gas fraction. The critical densities of HCN, HNC, and HCO^+ are all $n_{cr} > 10^5\,cm^{-3}$ for the $J = 1 - 0$ transition (Loenen et al. 2007), which is significantly higher than CO $J = 1 - 0$ ($n_{cr} \sim 3 \times 10^3\,cm^{-3}$; Loenen et al. 2007).

Because HCN, HNC, and HCO^+ in the $J = 1 - 0$ transition all have similar critical densities, the relative strengths of the lines of these molecules are driven largely by ongoing physical processes. Infrared (IR) pumping can enhance HCN emission in a system with a strong background mid-IR field (Sakamoto et al. 2010), while HCO^+ can be destroyed via dissociative recombination in the presence of a significant abundance of electrons. HCN and HNC are isotopomers, and their relative abundance is driven by the temperature of the dense molecular gas (Talbi et al. 1996). Line ratios of these molecules can be used as a diagnostic for cosmic rays (Meijerink et al. 2011), photon dominated regions (PDRs, Kazandjian et al. 2012), and mechanical heating (Loenen et al. 2008; Kazandjian et al. 2012). Thus, these lines can be used to study the distribution of dense molecular gas within a system and constrain the relative fraction of dense gas from region to region, as well as the relative importance of physical processes such as mechanical heating.

In this paper, we present observations of the $J = 1 - 0$ transition of HCN, HNC, and HCO^+ in the Antennae using ALMA. We adopt a distance to NGC 4038/39 of $D = 22$ Mpc (Schweizer et al. 2008), corresponding to an angular scale of 107 pc/″. We combine these observations with previous observations of CO $J = 1 - 0$ from Wilson et al. (2000, 2003). In this work, we detail the observations and data reduction in Section 2, and discuss separating the emission into the brightest regions in Section 3. We present various line ratios of HCN, HNC, HCO^+, and CO in Section 4, and discuss the implications of the measured line ratios in Section 5.

2. OBSERVATIONS

NGC 4038 was observed in two pointings over the course of two nights each in 2013 March and 2014 April as part of ALMA Cycle-1. One pointing was positioned to cover the nucleus of NGC 4038 and the western loop ($12^h01^m51\overset{s}{.}7763$, $-18°52'02\overset{''}{.}892$), while the other was positioned to cover both the overlap region and the nucleus of NGC 4039 ($12^h01^m54\overset{s}{.}5945$, $-18°52'50\overset{''}{.}891$), with a total on-source integration time of 20356 s. The antenna array configuration was C32-4. The bandpass calibrators used were J1256-0547, J1246-2547, and J1130-1449; J1215-1731 was used as the phase calibrator and Titan was used as the amplitude calibrator throughout.

Band 3 was used with one spectral window set to observe both HCN and HCO^+ simultaneously. A second spectral window was aligned to search for HNC emission throughout the Antennae. The total usable bandwidth for each of these spectral windows was 1875 MHz, with a channel spacing of 0.488 MHz. The two remaining spectral windows were centered at 101.0 and 102.875 GHz to observe the continuum emission across the Antennae. The bandwidth of the two continuum windows was 2000 MHz with a channel spacing of 15.625 MHz.

We reduce these data using the Common Astronomy Software Applications package version 4.2. We start by running the script provided to the PI as part of the data delivery to calibrate the *uv*-datasets before splitting out the target from the calibrated data set. We further split out the spectral window that contained the HCN and HCO^+ lines, and the spectral window that contained the HNC line. We subtract the background continuum emission by fitting a first order polynomial to the line-free channels of each spectral window using the `uvcontsub` task.

We create dirty data cubes for each of the HCN, HCO^+, and HNC $J = 1 - 0$ transitions with a channel width of 5 km s^{-1} and cell size of 0.″3. The restoring beams of the cleaned data cubes when using Briggs weighting with robust = 0.5 are $1\overset{''}{.}85 \times 1\overset{''}{.}51$, $-79\overset{°}{.}2$ for the HCO^+ line and $1\overset{''}{.}86 \times 1\overset{''}{.}52$, $-79\overset{°}{.}8$ for the HCN line (the HNC line was too weak to detect at the native ALMA resolution). We set the restoring beam for the HCN and HCO^+ transitions to the HCN beam and create clean data cubes by placing clean boxes around $>5\sigma$ emission in the dirty data cubes, being careful not to select artifacts. We clean down to a threshold of 1.1 mJy beam^{-1}, corresponding to 2σ in both dirty data cubes as measured in the line-free channels ($\sigma = 0.55$ mJy beam^{-1}).

In addition, we create dirty and clean data cubes to match the beam of the CO $J = 1 - 0$ data-cube from Wilson et al. (2000, 2003). We set the *uv*-taper on the outer baselines to $5\overset{''}{.}0 \times 2\overset{''}{.}0$, $1\overset{°}{.}45$ for HCN, HCO^+, and HNC with a restoring beam of $4\overset{''}{.}91 \times 3\overset{''}{.}15$, $1\overset{°}{.}45$. We use the same channel width and cell size as before, and draw clean boxes around the 5σ emission. We clean down to a threshold of 1.6 mJy beam^{-1}, corresponding to 2σ of the tapered dirty data cubes ($\sigma = 0.8$ mJy beam^{-1}).

We create moment maps that include emission above 2σ. The untapered moment-0 maps are shown in Figure 1, while the tapered moment-0 maps are shown in Figure 2, along with the CO $J = 1 - 0$ moment-0 map from Wilson et al. (2000, 2003). Finally, we correct all our HCN, HCO^+, and HNC moment-0 maps for the primary beam. The largest correction occurs in the nucleus of NGC 4039, where the primary beam correction is on the order of $\sim 0.6 - 0.7$ for both the native ALMA resolution maps and the CO $J = 1 - 0$ resolution maps. The CO $J = 1 - 0$ map from Wilson et al. (2003) has already been corrected for the primary beam.

Gao et al. (2001) observed the Antennae in HCN $J = 1 - 0$ in two pointings: one centered on the nucleus of NGC 4038 and the other on the brightest CO emission from the overlap region. The full-width half-maximum of their beam was $\sim 72''$ and their two pointings include both nuclei and the overlap region. They calculate a total HCN $J = 1 - 0$ luminosity of 0.8×10^8 K km s^{-1} pc^2 (adjusted to our adopted distance of 22 Mpc), while we measure a total of HCN $J = 1 - 0$ luminosity of $\sim 0.7 \times 10^8$ K km s^{-1} pc^2 in our ALMA maps.

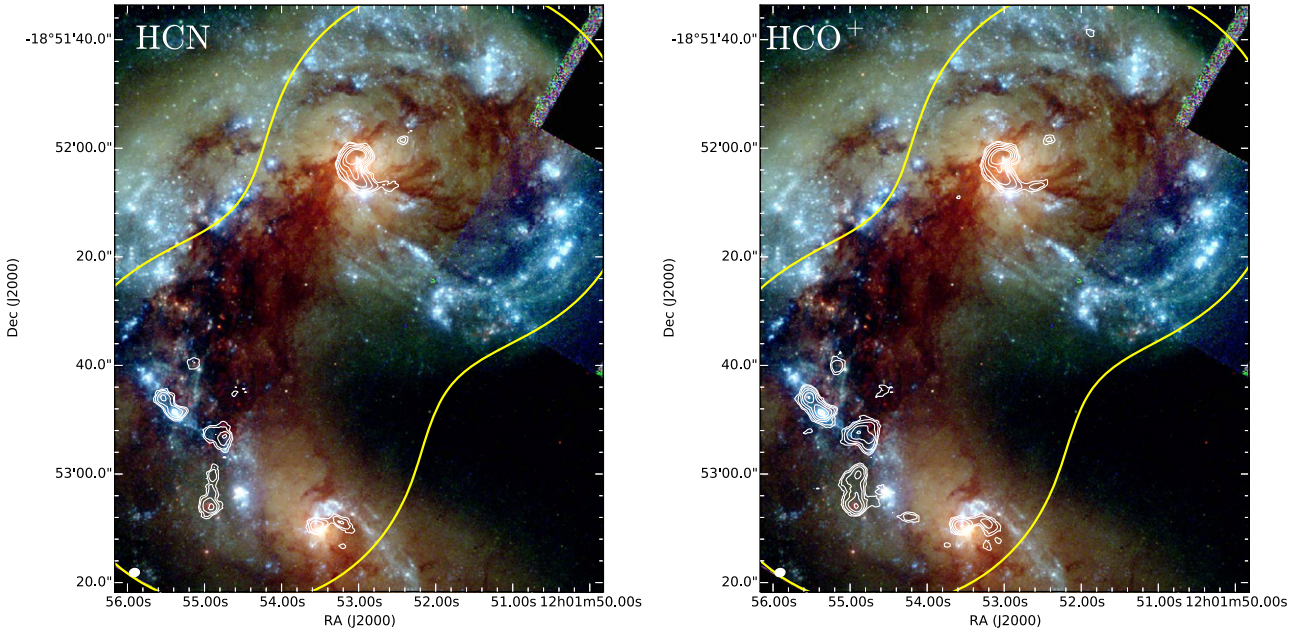


Figure 1. HCN (left) and HCO^+ (right) moment-0 contours overlaid on the same *HST* image of the Antennae. The contours shown have not been corrected for the primary beam. The *HST* image was created using data from Whitmore et al. (1999). The HCN and HCO^+ contours, shown in white, correspond to (3, 5, 9, 15, 25, 35) × (2.8 × 10^{-2} Jy beam^{-1} km s^{-1}). The beam of the dense gas tracer observations is shown by a white ellipse in the lower-left corner. The combined half-power beam width of the two pointings is shown by the yellow contour.

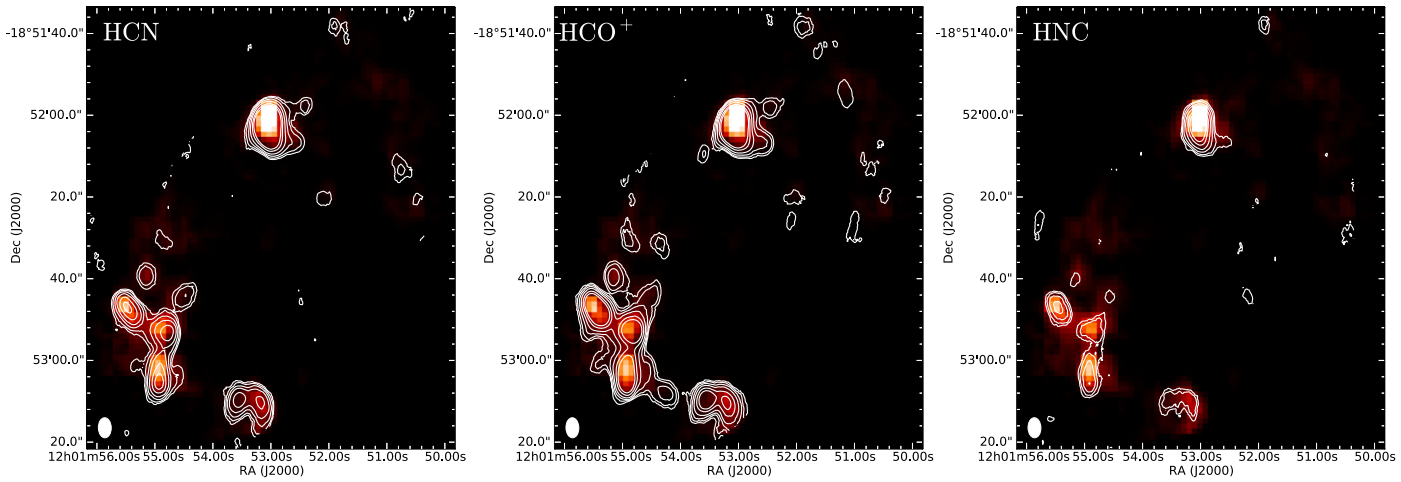


Figure 2. HCN (left), HCO^+ (middle), and HNC (right) moment-0 contours beam matched to the CO $J = 1 - 0$ observations from Wilson et al. (2003) overlaid on the same CO $J = 1 - 0$ moment-0 map. The contours correspond to (3, 5, 9, 15, 25, 35) × (3.6 × 10^{-2} Jy beam^{-1} km s^{-1}). The beam is shown by the white ellipse in the lower-left corner of each image. These contours have been corrected for the fall-off in sensitivity due to the primary beam.

Our detected HCN emission is well within their two beams, and we do not expect significant HCN emission outside our observed region. This comparison suggests that we recover ∼90% of the total HCN emission in our ALMA observations.

We estimate the measurement uncertainties in our moment maps by first determining the number of channels included in each pixel of the moment map ($N_{\rm chan}$). We calculate the uncertainty in each pixel as $\sqrt{N_{\rm chan}}\,\sigma\Delta v$, where σ is the root-mean squared uncertainty measured from our line-free channels of the data cubes, and $\Delta v = 5$ km s^{-1} is the channel width. Furthermore, when comparing our dense gas tracers to our CO $J = 1 - 0$ map, we add a 5% calibration uncertainty.[4] The calibration uncertainty of the CO $J = 1 - 0$ map is 20% (Wilson et al. 2003). While individual luminosities can vary depending on the size of the aperture chosen, line ratios measured in the same apertures from maps with the same beam size should be quite accurate measures of the average line ratio over a given region. Line ratios involving the HNC line may be somewhat more uncertain because this is the weakest line and the 2σ clipping used to make the moment maps is a larger fraction of the peak flux.

3. THE BRIGHTEST REGIONS IN THE ANTENNAE

In this paper we focus on the HCN, HNC, and HCO^+ emission from the brightest regions in the Antennae. A full catalog of clouds in HCN, HNC, and HCO^+ will be published in a future paper, along with a cloud-by-cloud analysis of the emission.

[4] ALMA Cycle 1 Technical Handbook. Available at https://almascience.nrao.edu/documents-and-tools/cycle-1/alma-technical-handbook.

Table 1
Measured Flux Densities of The Molecular Lines

Region ID	S_{HCN}[a] (Jy km s^{-1})	S_{HCO+}[a] (Jy km s^{-1})	S_{HNC}[a] (Jy km s^{-1})	S_{CO}[b] (Jy km s^{-1})
NGC 4038	14.32 ± 0.08	14.23 ± 0.08	5.58 ± 0.06	290 ± 5
NGC 4039	4.03 ± 0.08	6.51 ± 0.09	1.06 ± 0.05	100 ± 5
SGMC 1	2.59 ± 0.05	6.63 ± 0.06	1.01 ± 0.04	117 ± 2
SGMC 2	2.12 ± 0.04	4.50 ± 0.05	0.59 ± 0.03	92 ± 2
SGMC 3	0.69 ± 0.03	1.82 ± 0.03	0.25 ± 0.02	61 ± 2
SGMC 4	1.32 ± 0.03	3.03 ± 0.04	0.46 ± 0.02	67 ± 3
SGMC 5	0.94 ± 0.03	1.35 ± 0.03	0.30 ± 0.02	30 ± 2
SGMC 3+4+5	3.34 ± 0.06	6.18 ± 0.06	1.10 ± 0.04	128 ± 3
C6	0.40 ± 0.02	0.45 ± 0.02	0.14 ± 0.01	15 ± 1
C7	0.34 ± 0.02	0.53 ± 0.02	0.13 ± 0.01	22.5 ± 0.8

Notes. The reported uncertainties are the measurement uncertainties. To convert into luminosity with units of K km s^{-1} pc^2, multiply fluxes by $1.5666 \times 10^{10}(\nu_0/\mathrm{GHz})^{-2}$. See text for additional details.
[a] The calibration uncertainty for ALMA band 3 in Cycle 1 is 5% (see text).
[b] The calibration uncertainty for the CO observations is 20% (see text and Wilson et al. 2003).

Wilson et al. (2000) identified and isolated the seven brightest regions in their CO $J = 1 - 0$ map of the Antennae using the clump identification algorithm CLFIND (Williams et al. 1994). These regions include both nuclei (NGC 4038 and NGC 4039) and five large clouds in the overlap region, dubbed Super Giant Molecular Complexes (SGMCs). In addition to these seven regions, we identify two additional bright regions: C6 and C7. These clouds correspond to clouds 16, 17, and 18 (C6) and clouds 67 and 74 (C7) in the CO cloud catalog published in Wilson et al. (2003).

We place elliptical apertures around each of the nine brightest regions to measure the total HCN, HNC, HCO$^+$, and CO fluxes (S_{mol}, Table 1) in the moment-0 map for the $J = 1 - 0$ transition for each molecule (Figure 3). The total fluxes and total luminosities of the nuclei, SGMCs, and clouds C6 and C7 are measured at the CO $J = 1 - 0$ resolution for all four molecules.

For the five SGMC regions, we are unable to distinguish between SGMC 3, 4, and 5 in the moment-0 map, and so we combine these three SGMCs into SGMC 3 + 4 + 5. However, we can distinguish between them in velocity-space, as shown in Wilson et al. (2000; see their Figure 5). Using the measured local standard of rest velocity (V_{lsr}) along with the velocity widths (ΔV_{FWHM}) from Wilson et al. (2000), we create moment-0 maps for the velocity range spanned by each SGMC. We measure the flux and luminosity for each cloud in their own moment-0 map using the same aperture as used for SGMC 3+4+5. There are two channels of overlap in the velocity ranges for SGMC 4 and 5 as measured by Wilson et al. (2000); we separate the two SGMCs by including one channel in each of the moment maps of SGMC 4 and 5.

Johnson et al. (2015) identified a small region in SGMC 2 in their ALMA CO $J = 3 - 2$ map of the overlap region that they believe to be the precursor to a SSC; we have dubbed this region "pre-SSC" in this work. The resolution of their CO $J = 3 - 2$ map is considerably better than that of our observations (beam size $= 0\farcs56 \times 0\farcs43$), while the size of the pre-SSC as measured using the CPROPS program (Rosolowsky & Leroy 2006) is $\sim 0\farcs66 \times 0\farcs55$, which is less than the size of the beam of our HCN and HCO$^+$ observations. We created a moment-0 map using the velocity range measured for the pre-SSC by Johnson et al. (2015) and our data cubes at the native ALMA resolution. However, even in this map the pre-SSC is not visible as a separate source. The HCN and HCO$^+$ peak fluxes measured at the location of the pre-SSC are 0.28 and 0.45 Jy beam^{-1} km s^{-1}, respectively; however, these fluxes almost certainly contain significant contamination from SGMC 2 and so should be regarded as upper limits to the true flux of the pre-SSC.

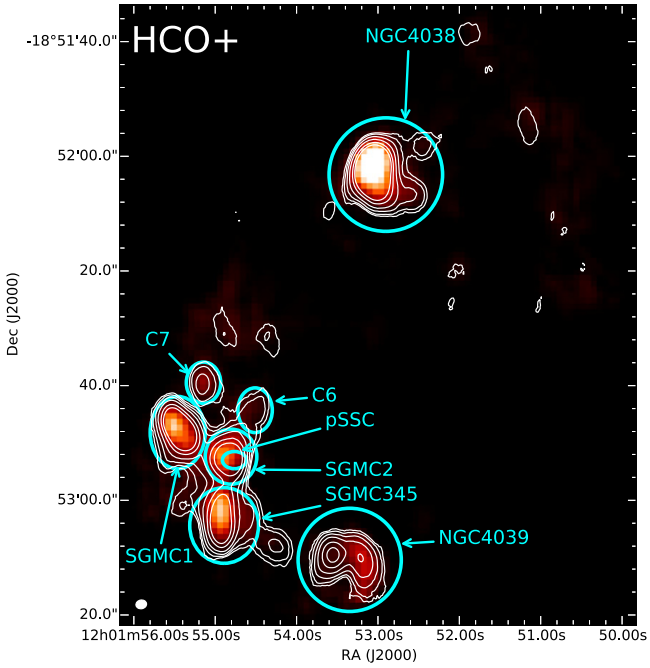


Figure 3. Map of the brightest regions in the Antennae. The background image is the CO $J = 1 - 0$ map from Wilson et al. (2000), and the HCO$^+$ $J = 1 - 0$ contours from Figure 2 are overlaid. The cyan ellipses indicate the location of the two nuclei, the five SGMCs, and the two additional clouds (C6 and C7), along with the precursor super star cluster "pSSC."

4. LINE RATIOS

We calculate the HCN/HCO$^+$ and HCN/CO line-ratio maps for both the native resolution and CO beam matched moment-0 maps by dividing the moment-0 maps directly (Figure 4). The difference between the primary beam correction for the HCN and HCO$^+$ moment-0 maps is minimal, so we use the nonprimary beam-corrected maps for this line ratio. For the line ratio of HCN/CO, we use the primary beam-corrected maps. In addition, we include only pixels with a 3σ detection of both molecular transitions in the moment-0 maps.

4.1. Ratios of The Dense Gas Tracers

We calculate the ratios of the luminosities of the dense gas tracers HCN, HNC, and HCO$^+$ for the brightest regions in the Antennae (see Section 3). We use the fluxes that we measure in Table 1 at the OVRO beam size, and convert them to luminosities using the following formula (Wilson et al. 2008)

$$\frac{L'}{\mathrm{K\ km\ s^{-1}\ pc^2}} = 3.2546 \times 10^7 \left(\frac{S_{\mathrm{mol}}}{\mathrm{Jy\ km\ s^{-1}}}\right)\left(\frac{D_L}{\mathrm{Mpc}}\right)^2 \times \left(\frac{\nu_0}{\mathrm{GHz}}\right)^{-2}(1+z)^{-1} \quad (1)$$

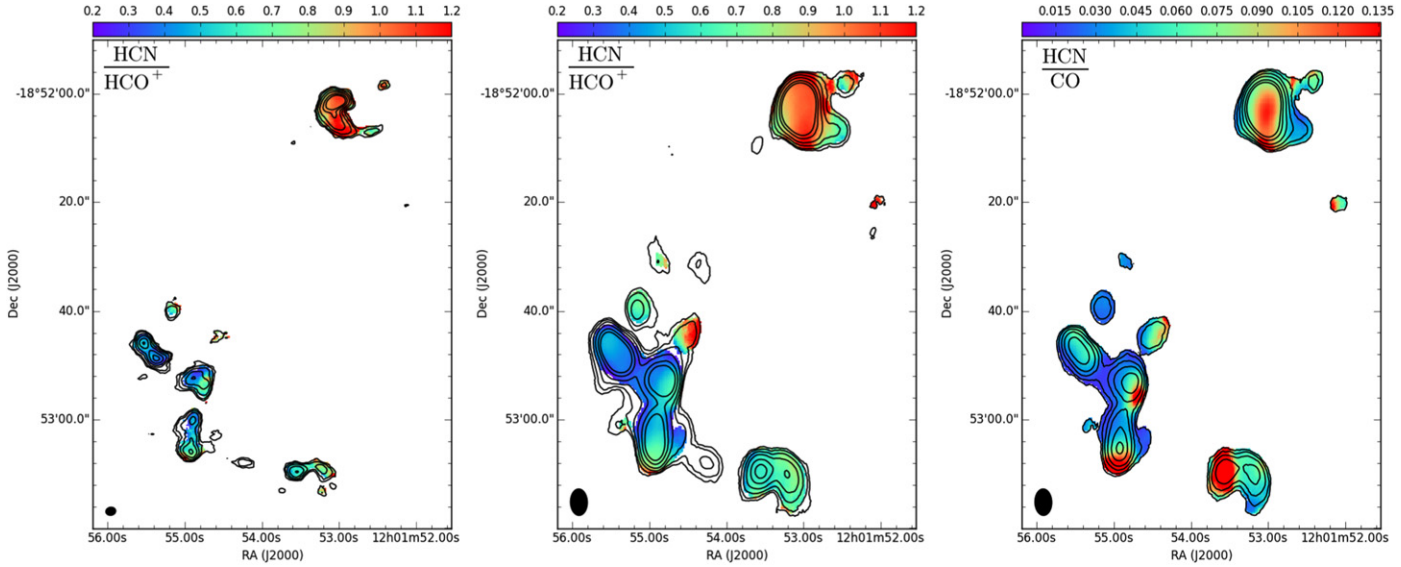


Figure 4. HCN/HCO$^+$ intensity ratio maps at the native ALMA beam (left) and CO $J = 1 - 0$ beam (middle), along with the HCN/CO intensity ratio map (right). The HCO$^+$ contours from Figure 1 (left) and Figure 2 (middle) are overlaid on the left and middle line-ratio maps, while the HCN contours from Figure 2 (left) are overlaid on the right line-ratio map. The nucleus of NGC 4038 exhibits the highest ratio of HCN/HCO$^+$(~1), while the same line ratio in the overlap region is about a factor of two smaller.

Table 2
Luminosity Ratios for The Brightest Regions in The Antennae

Region ID	L_{HCN}/L_{HCO+}	L_{HNC}/L_{HCO+}	L_{HNC}/L_{HCN}	L_{HCN}/L_{CO}	L_{HCO+}/L_{CO}	L_{HNC}/L_{CO}
NGC 4038	1.019 ± 0.008	0.384 ± 0.005	0.377 ± 0.005	0.083 ± 0.001	0.082 ± 0.001	0.0314 ± 0.0006
NGC 4039	0.63 ± 0.02	0.160 ± 0.008	0.25 ± 0.01	0.068 ± 0.004	0.109 ± 0.006	0.017 ± 0.001
SGMC 1	0.396 ± 0.008	0.149 ± 0.006	0.38 ± 0.02	0.0376 ± 0.0009	0.095 ± 0.002	0.0142 ± 0.0006
SGMC 2	0.48 ± 0.01	0.128 ± 0.006	0.27 ± 0.01	0.039 ± 0.001	0.082 ± 0.002	0.0105 ± 0.0006
SGMC 3	0.39 ± 0.02	0.132 ± 0.010	0.34 ± 0.03	0.019 ± 0.001	0.050 ± 0.002	0.0066 ± 0.0005
SGMC 4	0.44 ± 0.01	0.149 ± 0.008	0.34 ± 0.02	0.033 ± 0.002	0.075 ± 0.003	0.0111 ± 0.0008
SGMC 5	0.70 ± 0.03	0.22 ± 0.02	0.31 ± 0.02	0.053 ± 0.005	0.075 ± 0.006	0.016 ± 0.002
SGMC 3+4+5	0.55 ± 0.01	0.173 ± 0.006	0.32 ± 0.01	0.044 ± 0.001	0.081 ± 0.002	0.0140 ± 0.0006
C6	0.90 ± 0.07	0.29 ± 0.03	0.33 ± 0.04	0.047 ± 0.005	0.052 ± 0.005	0.015 ± 0.002
C7	0.65 ± 0.05	0.24 ± 0.03	0.36 ± 0.04	0.026 ± 0.002	0.039 ± 0.002	0.009 ± 0.001

Note. The reported uncertainties are measurement uncertainties only, which are equal to the total uncertainty for the ratios that include only HCN, HCO$^+$, and HNC. The uncertainties in the line ratios that include CO are dominated by the calibration uncertainties. We add the calibration uncertainties from the two instruments in quadrature to obtain a total line-ratio uncertainty of 21%. See the text for additional details.

where S_{mol} is the flux, $D_L = 22$ Mpc is the distance, ν_0 is the rest frequency of the transition, and $z = 0.005477$ is the redshift. We show the ratios of L_{HNC}/L_{HCN}, L_{HNC}/L_{HCO+}, and L_{HCN}/L_{HCO+} in Table 2 and plot the ratios of L_{HNC}/L_{HCO+} and L_{HCN}/L_{HCO+} in Figure 5.

With the exception of C6, the nucleus of NGC 4038 shows values of L_{HCN}/L_{HCO+} and L_{HNC}/L_{HCO+} that are more than 1.5 times greater than the other regions. For C6, the ratios of L_{HCN}/L_{HCO+} and L_{HNC}/L_{HCO+} are only ~1.1 and ~1.3 times less than in NGC 4038, respectively. Of the remaining regions, SGMCs 1, 2, 3, and 4 exhibit similar values for both the ratio of L_{HCN}/L_{HCO+} (~0.39–0.48) and the ratio of L_{HNC}/L_{HCO+} (~0.13–0.15), suggesting similar dense gas properties across the four regions. The nucleus of NGC 4039 exhibits slightly larger values for both ($L_{HCN}/L_{HCO+} \sim 0.63$, $L_{HNC}/L_{HCO+} \sim 0.16$). Of the SGMCs, SGMC 5 exhibits the largest value for both line ratios (L_{HCN}/L_{HCO+}~0.7 and $L_{HNC}/L_{HCO+} \sim 0.22$); this enhanced line ratio can also be seen in the high-velocity end of the spectrum for this region in Bigiel et al. (2015).

The value of L_{HNC}/L_{HCN} varies by less than a factor of 1.5 across all nine regions. The largest deviations occur for the nucleus of NGC 4039 and SGMC 2, with $L_{HNC}/L_{HCN} = 0.25$ and $L_{HNC}/L_{HCN} = 0.27$, respectively. Of the remaining eight regions, L_{HNC}/L_{HCN} is nearly constant, varying by only ~20% ($L_{HNC}/L_{HCN} \sim 0.31$–$0.38$).

4.2. Ratios to CO

The ratio of the detected dense gas tracers to the total CO luminosity is an indicator of the fraction of the dense molecular gas within the different regions in the Antennae. We calculate this ratio for all three dense gas tracers relative to CO (Table 2), and plot the ratio of L_{HCN}/L_{CO} and L_{HCO+}/L_{CO} in Figure 6.

The ratio of L_{HCN}/L_{CO} varies by more than a factor of four, with the two nuclei exhibiting larger values than the other regions in the Antennae. The smallest values are seen in SGMC 3 and C7, while the remaining six regions have values ~0.04. The ratio of L_{HCO+}/L_{CO}, on the other hand, varies by a factor of ~2.5. Once again, SGMC 3 and C7, along with C6, show the

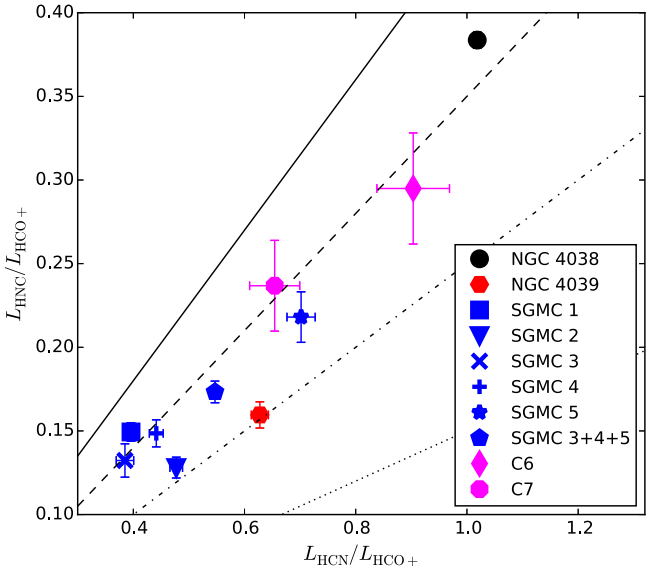


Figure 5. Luminosity ratios of the dense gas tracers for the brightest regions in the Antennae calculated at the CO $J = 1 - 0$ beam. The error bars correspond to measurement uncertainties in the line ratios. The lines correspond to the lines of constant $L_{\rm HNC}/L_{\rm HCN}$, with $L_{\rm HNC}/L_{\rm HCN} =$ 0.15 (dotted line), 0.25 (dash–dot line), 0.35 (dashed line), and 0.45 (solid line). The region SGMC 3+4+5 corresponds to the region in the moment-0 map spanned by SGMC 3, 4, and 5, while the values for SGMC 3, 4, and 5 were calculated from moment maps created based on the velocity range calculated in Wilson et al. (2000)

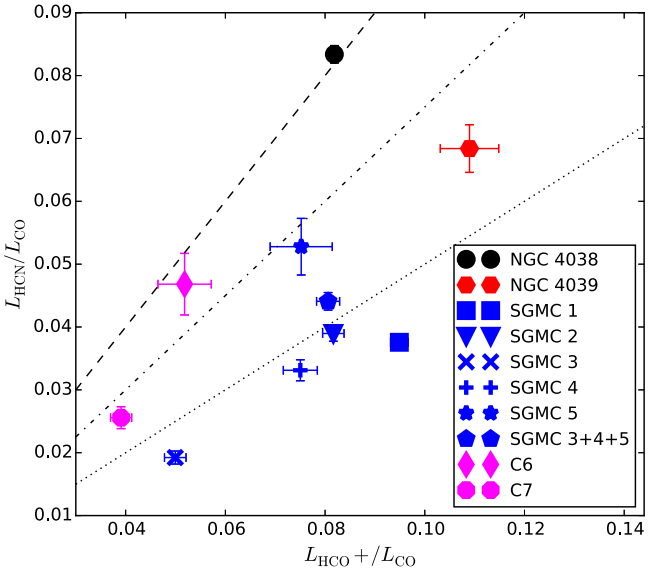


Figure 6. Plot of the dense gas fraction calculated at the CO $J = 1 - 0$ beam using $L_{\rm HCN}/L_{\rm CO}$ (y-axis) and $L_{\rm HCO+}/L_{\rm CO}$ (x-axis) for the brightest regions in the Antennae. The errors bars correspond to the measurement uncertainties in the ratios, while the calibration uncertainty of these line ratios is ∼21%. The lines correspond to lines of constant $L_{\rm HCN}/L_{\rm HCO+}$, with $L_{\rm HCN}/L_{\rm HCO+} = 0.5$ (dotted line), 0.75 (dashed–dotted line), and 1.0 (dashed line). The region SGMC 3+4+5 corresponds to the region in the moment-0 map spanned by SGMC 3, 4, and 5, while the values for SGMC 3, 4, and 5 were calculated from moment maps based on the velocity range calculated in Wilson et al. (2000)

smallest values of $L_{\rm HCO+}/L_{\rm CO}$ (∼0.04–0.05), while the nucleus of NGC 4039 has the highest ratio of $L_{\rm HCO+}/L_{\rm CO}$ (∼0.1). The remaining regions, including the nucleus of NGC 4038, all have a characteristic value of $L_{\rm HCO+}/L_{\rm CO}$ of ∼0.08.

5. DISCUSSION

5.1. On The Global Line Ratio of $L_{\rm HCN}/L_{\rm CO}$

Gao et al. (2001) measured the HCN $J = 1 - 0$ emission at two locations in the Antennae with a beam FWHM = 72″: the nucleus of NGC 4038 and the overlap region, including a large portion of NGC 4039. They calculated a global value of $L_{\rm HCN}/L_{\rm CO} = 0.02$. This is comparable to the value we calculate for SGMC 3 ($L_{\rm HCN}/L_{\rm CO} = 0.019$), the smallest value of our nine regions. $L_{\rm HCN}/L_{\rm CO}$ ratios in five of our regions are a factor of two or more larger than the global value calculated by Gao et al. (2001), while the value calculated for the nucleus of NGC 4038 is a factor of four larger.

There are two major contributions that could lead to such a large difference in our ratios compared to the global ratio from Gao et al. (2001): missing flux in the CO interferometric observations and CO emitting gas beyond the boundaries of our defined regions. Wilson et al. (2003) compared their interferometric map of CO $J = 1 - 0$ to the same region in the Gao et al. (2001) single-dish map and found that only ∼65% of the flux is recovered in the interferometric map. In comparison, we determined that most of the HCN emission is recovered in our map (see Section 2).

The total CO luminosity in our interferometric map from the seven brightest regions (with SGMC 3, 4, and 5 combined as SGMC 3+4+5) is $L_{\rm CO} = 9.0 \times 10^8$ K km s^{-1} pc^2, whereas the total luminosity over the same area from the single-dish map used in Gao et al. (2001), scaled to our adopted distance of 22 Mpc, is $L^G_{\rm CO} = 19.5 \times 10^8$ K km s^{-1} pc^2 (Wilson et al. 2003). Similarly, the total HCN luminosity from our regions is $L_{\rm HCN} = 5.4 \times 10^7$ K km s^{-1} pc^2, whereas Gao et al. (2001) measure $L^G_{\rm HCN} = 8 \times 10^7$ K km s^{-1} pc^2. Based on this, ∼68% of the total HCN emission originates from the brightest regions of the Antennae, while only ∼46% of the total CO emission originates from these same regions.

If we assume that the ∼32% of the HCN emission found outside these regions is associated with CO emission, we can assume a ratio of $L_{\rm HCN}/L_{\rm CO} \sim 0.04$ and calculate that these regions account for another ∼33% of the total CO emission. This leaves ∼21% of the CO emission unaccounted for and presumably not within relatively dense GMCs or producing significant HCN emission. If we instead adopted the global value for $L_{\rm HCN}/L_{\rm CO}$ of 0.02 from Gao et al. (2001), then all the CO emission would originate in GMCs producing significant HCN emission. Thus, the amount of CO emission in the Antennae associated with diffuse molecular gas is ⩽20%.

Using the CO $J = 1 - 0$ map of M51 from the Plateau de Bure interferometer (PdBI) Arcsecond Whirlpool Survey (PAWS), Pety et al. (2013) identified an extended, diffuse component of the molecular gas that accounts for ∼50% of the flux, and in which CO $J = 1 - 0$ emission is subthermally excited. It is possible that a significant fraction of the 21% of the CO emission that is unaccounted for in NGC 4038/39 is subthermally excited CO from a diffuse, extended component, such as in M51. The critical density of the CO $J = 1 - 0$ transition ($n_{\rm cr} \sim 10^3$ cm^{-1}) is significantly less than that of HCN ($n_{\rm cr} \sim 10^5$ cm^{-1}), so we would not expect any HCN emission from an extended, diffuse component. This would lead to a suppression of the global $L_{\rm HCN}/L_{\rm CO}$ ratio when compared to smaller regions. High-resolution, flux-recovered observations of CO $J = 1 - 0$ in the Antennae using ALMA would allow us to detect the presence of this extended diffuse component.

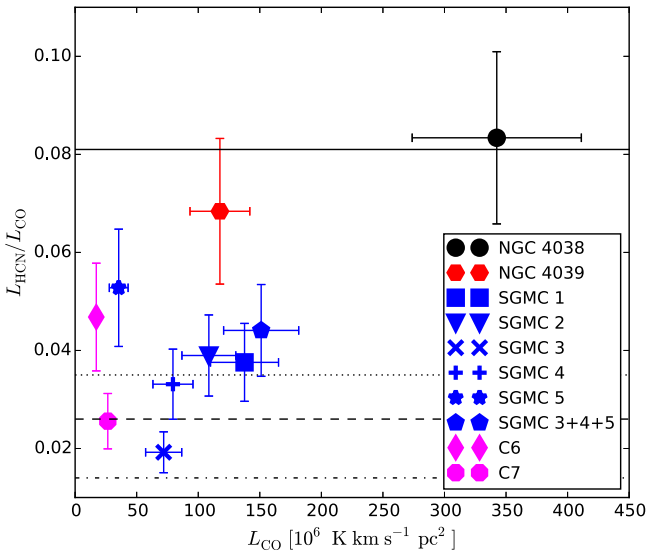


Figure 7. Dense gas fraction as measured by L_{HCN}/L_{CO} (*y*-axis) as a function of CO luminosity (*x*-axis). The data points are the values measured for the brightest regions in the Antennae, while the error bars correspond to the measurement uncertainty and the calibration uncertainty added in quadrature. The solid and dashed horizontal lines correspond to the average values of L_{HCN}/L_{HCO+} as measured in the bulge and plane of the Milky Way, while the dotted–dashed line corresponds to the average value measured in local GMCs (Helfer & Blitz 1997a). The dashed line corresponds to typical values of L_{HCN}/L_{HCO+} in normal spiral galaxies (Gao & Solomon 2004b; Graciá-Carpio et al. 2006).

5.2. Dense Gas Fraction

We use the ratio of L_{HCN}/L_{CO} as an indicator of the dense gas fraction throughout the Antennae, and show this ratio compared to L_{CO} in Figure 7 for the nine brightest regions in the Antennae. The typical values for normal spiral galaxies are $L_{HCN}/L_{CO} \sim 0.02$–0.05 (Gao & Solomon 2004a, 2004b), and this fraction can increase to $L_{HCN}/L_{CO} > 0.06$ in the case of some extreme star-forming LIRGs and ULIRGs.

The two nuclei, NGC 4038 and NGC 4039, show a higher dense gas fraction than the rest of the system by roughly a factor of $\sim 2-3$. In comparison, Helfer & Blitz (1997a) measured I_{HCN}/I_{CO}—which is comparable to L_{HCN}/L_{CO}—in the plane of the Milky Way and found that the dense gas fraction was greater toward the bulge ($I_{HCN}/I_{CO} \sim 0.081$) than the rest of the plane ($I_{HCN}/I_{CO} \sim 0.026$). Helfer & Blitz (1997b) saw a similar increase in NGC 6946, a grand-design spiral galaxy, and NGC 1068, a Seyfert-2 galaxy with a starburst, with the ratio of I_{HCN}/I_{CO} increasing by a factor of 5–10 toward the bulge. In larger surveys extending to higher infrared luminosities, Baan et al. (2008) reported I_{HCN}/I_{CO} ratios of 0.01 to 0.18 with a median spatial resolution of 5 kpc in their sample of ∼75 galaxies. García-Burillo et al. (2012) found ratios from 0.02 to 1 in a sample of ∼130 galaxies, with higher ratios more common in galaxies with infrared luminosities above 10^{11} $L_\odot$. Juneau et al. (2009) found ratios of 0.02 to 0.06 in galaxies with infrared luminosities in the range 10^{10}–10^{11} $L_\odot$. Recently, Usero et al. (2015) surveyed 62 positions in the disks of normal spiral galaxies, and found I_{HCN}/I_{CO} ratios of 0.011 to 0.065 on average scales of 1.5 kpc; this line ratio correlates with both the atomic-to-molecular gas fraction and the stellar surface density.

Helfer & Blitz (1997a) argued that the increased dense gas fraction in the bulge is due to an increase in the average gas pressure toward the center of the Milky Way, with $I_{HCN}/I_{CO} \propto P^{0.19}$. With this relation, a factor of two difference in the ratio of I_{HCN}/I_{CO} would correspond to a factor of ∼40 difference in the average gas pressure. This increase in gas pressure is due in part to the increased stellar density in the bulge, which increases the gravitational potential and in turn increases the gas pressure required to support the hydrostatic equilibrium. As in the Milky Way, the high ratio of I_{HCN}/I_{CO} seen in the two nuclei of the Antennae could be due to an increase in the stellar density compared with the overlap region.

Schirm et al. (2014) calculated the pressure using a non-LTE excitation analysis of CO and [CI] in NGC 4038, NGC 4039, and the overlap region in relatively large beams (FWHM ∼43″, ∼5 kpc). Their cold component results suggest that the pressure in all three regions is similar ($P \sim 10^{4.5} - 10^{5.5}$ K cm^{-2}); however the 1σ ranges span an order of magnitude. (It is important to note that, due to the large beams, NGC 4039 contains some emission from the overlap region, which may be reflected in the non-LTE excitation analysis.) Their warm component, traced largely by the CO $J = 7 - 6$ and $J = 8 - 7$ transitions, shows a much higher pressure in NGC 4038 ($P \sim 10^9$ K cm^{-2}) than in either NGC 4039 or the overlap region ($P \sim 10^{7.5}$ K cm^{-2}).

It is possible that some, or even most, of the HCN emission is associated with their warm component; however, the $J = 1 - 0$ transition is often associated with cold, dense gas. Observations of higher J HCN and HNC transitions coupled with a non-LTE excitation analysis similar to the method used by Schirm et al. (2014) would help determine whether this HCN emission is associated with cold or warm dense molecular gas, while also enabling direct calculations of the pressure in the dense gas in these regions.

We show the ratio of I_{HCN}/I_{CO} in Figure 4 (right). In both NGC 4038 and NGC 4039, there is a region toward the very center where the ratio of I_{HCN}/I_{CO} increases by a factor of ∼2 compared to the surrounding regions. These high ratio regions are approximately the size of the CO beam, which corresponds to ∼500 pc, and is similar to the size of the bulges measured by Helfer & Blitz (1997b). Interestingly, the peak value of I_{HCN}/I_{CO} is greater in NGC 4039 than in NGC 4038, whereas averaged over the whole region the dense gas fraction is greater in NGC 4038.

In the overlap region, most of the molecular gas is characteristic of SGMC 1, where $L_{HCN}/L_{CO} \sim 0.04$. There are two interesting peaks in the distribution of the dense gas ratio in the overlap region: one in the southwest of SGMC 2, and another to the south of SGMC 3+4+5. The center of the peak in SGMC 2 is offset from the center of pre-SSC by ∼3″–4″, which corresponds to roughly a beam. Both peaks exhibit a higher ratio of I_{HCO+}/I_{CO} and, to a lesser extent, I_{HCN}/I_{HCO+} (Figure 8). No significant emission is detected at a 3σ level at either peak in either HCN or HCO$^+$ at the native ALMA resolution. However, both peaks are detected in the CO beam-matched maps of both dense gas tracers at a 5σ level. Moreover, there is also no obvious CO $J = 3 - 2$ emission detected at this location (Whitmore et al. 2014). It is possible that these high regions are produced by edge effects; inspection of the individual emission maps shows that the peaks of the HCN and the CO emission are not precisely coincident in these areas.

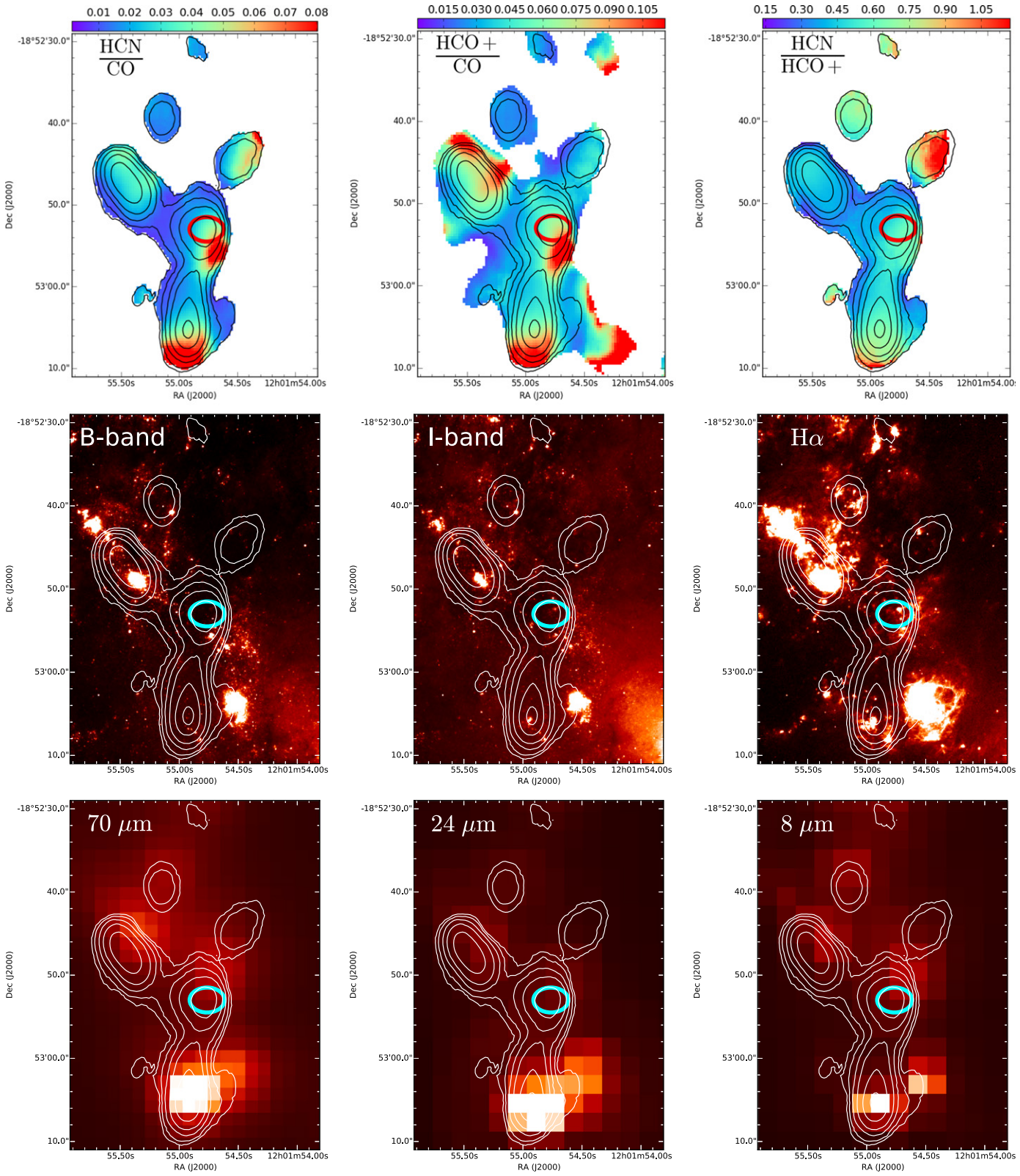


Figure 8. HCN contours beam matched to the CO observations overlaid on various ratio maps and emission maps. The contours correspond to (3, 5, 9, 15, 25, 35) × (3.6×10^{-2} Jy beam^{-1} km s^{-1}). Top row: line-ratio maps for HCN/CO (left), HCO$^+$/CO (middle), and HCN/HCO$^+$ (right). Middle row: *Hubble Space Telescope* images of the B-band (F435W, left), I-band (F814W, middle), and Hα (F658N, right) emission from Whitmore et al. (2010). Bottom row: *Herschel* PACS 70 μm emission from Klaas et al. (2010; left), *Spitzer* MIPS 24 μm emission (middle), and *Spitzer* IRAC 8 μm emission (right), all of which trace star formation. The location of the pre-SSC is shown by the red (top row) and cyan (bottom row) ellipses. None of the emission maps have any significant emission toward the high-dense fraction regions as traced by HCN/CO in the overlap region (see the text for more details).

5.3. Comparison to Other Wavelengths

Whitmore et al. (2010) observed the Antennae with the *HST* using multiple filters, including F435W, F814W, and F658N, which correspond to B-band, I-band, and Hα emission. We compare the HCN emission to each of these filters in the middle row of Figure 8. At the two peaks in the I_{HCO+}/I_{CO} ratio discussed in the previous section, there are only faint or no B-band or I-band optical counterparts. However, there is some nearby Hα emission at the southern edge of the SGMC 3+4+5 peak and near the eastern edge of the SGMC 2 peak. Furthermore, there is no 70 μm (Klaas et al. 2010), 24 μm (Zhang et al. 2010), or 8 μm (Wang et al. 2004) emission associated with the line-ratio peak near SGMC-2, although there is bright emission in these bands toward SGMC 3+4+5 that could have some relation to the southern peak in the line ratio (Figure 8).

The lack of emission in the B- and I-band images is likely due to high dust extinction in the overlap region. The 70 μm (Calzetti et al. 2010), 24 μm, and 8 μm (Wu et al. 2005a) fluxes all correlate strongly with star formation, so we attribute the deficiency in their emission to a lack of recent star formation within one or possibly both of the line-ratio peaks in the overlap region. As such, these high-dense gas fraction regions may be the result of turbulent motion due to the ongoing merger, and may indicate sites of future star formation within the overlap region.

5.4. Mechanical Heating and PDRs

HCN and HNC are isotopomers with similar excitation energies. The line ratio of L_{HNC}/L_{HCN} is driven in large part by their relative abundance, in which the exchange reaction H + HNC $\leftrightarrow$ H + HCN is an important factor (Schilke et al. 1992; Talbi et al. 1996). At temperatures $<$100 K, the rate coefficients of both the forward and reverse reactions are small, and this reaction is not important (Talbi et al. 1996). At temperatures of a few hundred K, the energies are sufficient to exceed the activation energy of the H + HNC reaction, leading to a higher relative abundance of HCN to HNC and a lower ratio of L_{HNC}/L_{HCN}.

It has been suggested that most molecular gas is in the form of PDRs (e.g., see the PDR model comparison study by Röllig et al. 2007). If mechanical heating is not included in the model, heating occurs only at the surface of the PDR, where the photon energies are high enough to liberate elections from the surfaces of dust grains. Recent PDR models have investigated the effects of mechanical heating on the molecular gas within PDRs (Meijerink et al. 2011; Kazandjian et al. 2012, 2015), in particular on the predicted atomic and molecular line ratios. They find that mechanical heating begins to have a measurable effect on the chemistry of the PDR, and consequently the line ratios, with contributions of as little as $\sim$1% to the total heating (Kazandjian et al. 2012).

In the Antennae, the ratio of L_{HNC}/L_{HCN} varies by less than a factor of 1.5 across the brightest regions, ranging from $\sim$0.25 to 0.38 (Table 2 and Figure 5). We compare our measured ratio with the PDR models with mechanical heating from Kazandjian et al. (2015). In their models, the mechanical heating is parameterized as α, which is equal to the total amount of mechanical heating relative to the PDR surface heating. For values of $\alpha < 0.05$, their reference models report a value of $L_{HNC}/L_{HCN} \geqslant 1$. Our measured line ratios are consistent with at least some (>5%) contribution of mechanical heating toward the total heating budget in all the bright regions in the Antennae.

In comparison, Schirm et al. (2014) modeled various line ratios of CO from $J = 1 - 0$ to $J = 8 - 7$, along with the FIR luminosity using PDR models that did not include mechanical heating. In all three regions, they found that the line ratios of the low-J CO transitions ($J = 1 - 0$ to $J = 3 - 2$) are consistent with a "cold" PDR with a field strength of $G_0 \sim 100$ and a molecular gas density of $n(H_2) \sim 10^3 - 10^4$ cm^{-3}. Line ratios of the high-J CO transitions ($J = 6 - 5$ to $J = 8 - 7$) are consistent with a "warm" PDR with a field strength of $G_0 \sim 1000$ and a molecular gas density of $n(H_2) \sim 10^4 - 10^5$ cm^{-3}, whereas the warm PDR accounts for $\sim$1% of the total molecular gas mass. Their warm PDR solutions are similar to model M3 from Kazandjian et al. (2015), for which $L_{HNC}/L_{HCN} \sim 1$ for all amounts of mechanical heating, whereas the field strength of their cold PDR models lies outside the range of G_0 modeled by Kazandjian et al. (2015). Future PDR modeling within the Antennae should include mechanical heating because it has to have a fundamental effect on the chemistry within these regions.

The higher ratio of L_{HNC}/L_{HCN} seen in the nucleus of NGC 4038 and SGMC 1 indicates that the relative contribution of mechanical heating is lower within these regions. Conversely, the lower ratio seen in the nucleus of NGC 4039 and SGMC 2 indicates a higher relative contribution of mechanical heating. An increase (decrease) in the relative contribution of mechanical heating could either be due to an increase (decrease) in the total mechanical heating, or a decrease (increase) in the total PDR surface heating. All four regions show similar star-formation efficiencies (SFEs), ranging from $2.19 L_\odot M_\odot^{-1}$ for NGC 4038 to $3.33 L_\odot M_\odot^{-1}$ for SGMC 2 (Klaas et al. 2010). As PDR surface heating is tied to the background FUV field strength emitted from young, massive stars, the similar SFEs within these four regions likely indicate variations in the amount of mechanical heating as opposed to the PDR surface heating. This, in turn, agrees with the results from Schirm et al. (2014) who found similar values for G_0 and $n(H_2)$ in NGC 4038, NGC 4039, and the overlap region.

Finally, our ratios of L_{HNC}/L_{HCN} are consistent with models from Kazandjian et al. (2015) with $\alpha > 0.1$ (while also consistent with $0.1 > \alpha > 0.05$). The molecular gas temperature of the models with $\alpha > 0.1$ is high ($T_{kin} > 100$ K), which would indicate that the HCN and HNC emission originates from a warm, dense molecular gas similar to the warm component found by Schirm et al. (2014). However, the $J = 1 - 0$ transition of both these molecules is typically assumed to be associated with cold, dense, star-forming molecular gas. It could be that this cold, dense gas is quickly heated by the ongoing star formation within these systems, via supernovae and stellar winds, or that the turbulent motion due to the ongoing merger heats this dense gas. A multi-transitional non-LTE excitation analysis can be used to assess whether the HCN and HNC $J = 1 - 0$ emission is from cold or warm dense gas.

5.5. Cosmic Rays and The Abundances of HCN and HCO$^+$

Differences in the ratio of HCN and HCO$^+$ of more than a factor of two are seen in both the total global line ratio in the form of L_{HCN}/L_{HCO+} (Table 2) and in the distribution of

I_{HCN}/I_{HCO+} (Figure 4). In particular, the nucleus of NGC 4038 exhibits a ratio ~1, while in the SGMCs the ratio is typically $\sim 0.4 - 0.6$. The differences in the line ratio suggest either different excitation conditions for the two molecules (e.g., see Juneau et al. 2009) or changes in the relative abundances. To look for varying excitation conditions, additional transitions are required of both molecules. Thus, we discuss the implications of varying abundances of HCN and HCO^+ in the context of the measured line ratios.

HCO^+ is an ion that is easily destroyed through recombination in the presence of free electrons. Free electrons can also combine with $HCNH^+$ to form HCN (Lintott & Viti 2006; Juneau et al. 2009), simultaneously enhancing the abundance of HCN while suppressing the abundance of HCO^+. These free electrons are generated in the formation of the H_3^+ ion, which occurs via $2H_2 + \zeta \rightarrow H_3^+ + H + e^-$ (McCall et al. 2003). Papadopoulos (2007) argued that deep within molecular clouds, where the dense gas is found, this reaction with cosmic rays is the primary source of free electrons; however H_3^+ is also important in the formation of HCO^+. Thus, interpreting variations in the line ratio of HCN and HCO^+ is not as straightforward as, say, HNC and HCN.

Meijerink et al. (2011) investigated the effects of cosmic rays on the abundances of various molecules, atoms, and ions within PDRs. They modeled a dense ($n(H_2) = 10^{5.5}\,cm^{-3}$) PDR region with a strong background UV field ($10^5 G_0$), along with an intermediate density ($n(H_2) = 10^3\,cm^{-3}$) PDR with a PDR field strength of $G_0 = 10^3$. They varied the cosmic ray rate from $5 \times 10^{-17}\,s^{-1}$ to $5 \times 10^{-13}\,s^{-1}$. In the dense PDR, they found that the abundances of both HCN and HNC are insensitive to changes in the cosmic ray rates. The abundance of HCO^+, however, increases with increasing cosmic ray rates, except at very high cosmic ray rates. In the intermediate density PDR case, the HCO^+, HCN, and HNC abundances decrease with increasing cosmic ray rate.

Cosmic rays are assumed to originate largely from supernova remnants (Schulz et al. 2007). Neff & Ulvestad (2000) measured the supernova rate (ν_{SN}) across the Antennae using nonthermal radio sources that trace compact supvernova, and found a global rate of $\nu_{SN} \sim 0.2 - 0.3\,yr^{-1}$. Schirm et al. (2014) compared the location of these supernova to their ~43″ beams for NGC 4038, NGC 4039, and the overlap region, and determined that ~66% of the supernova originate from the overlap region, 14% from the nucleus of NGC 4038, and ~6% from the nucleus of NGC 4039. In our new ALMA maps, the HCO^+ emission in the overlap region covers roughly twice the area of HCO^+ emission in either of the two nuclei. Neff & Ulvestad (2000) identified 115 sources in their 6 cm map, of which they estimate 60% to be nonthermal sources; there are 18 sources bright enough for their spectral index to be measured with sufficient accuracy to show they are nonthermal. Comparing to their catalogs, the overlap region contains thirty-six sources, of which six are confirmed to be nonthermal, NGC 4038 has nine (four) sources, and NGC 4039 has five (one) sources. These source counts suggest that the surface density of supernova in the overlap region is 0.7–2 times that of NGC 4038, while the surface density in NGC 4039 is 0.3–0.6 times that of NGC 4038, with the lower values corresponding to sources with confirmed nonthermal spectral indices.

Unfortunately, there is no clear trend between the L_{HCN}/L_{HCO+} ratio and the supernova surface density among these three sources. If the overlap region has a higher supernova surface density than NGC 4038, this could produce an increase in the local cosmic ray rate. This could in turn explain the decreased ratio of L_{HCN}/L_{HCO+} found in the overlap region. However, NGC 4039 has a lower supernova surface density than either of the other two regions and yet exhibits an L_{HCN}/L_{HCO+} ratio that is more similar to that of the overlap region. An active galactic nucleus (AGN) can also be the source of cosmic rays (Pierre Auger Collaboration et al. 2007); however multi-wavelength studies of the Antennae suggest that there is no AGN at the center of NGC 4039 (Neff & Ulvestad 2000; Brandl et al. 2009; Ueda et al. 2012). Ueda et al. (2012) suggest that the high line ratio of CO $J = 3 - 2/J = 1 - 0$ seen in NGC 4039 is not due to star-formation activity, but could possibly be due to a hidden AGN. If that is the case, the lower value of L_{HCN}/L_{HCO+} seen in NGC 4039 could perhaps be explained by the presence of such a hidden AGN.

6. SUMMARY AND CONCLUSIONS

In this paper, we present high-resolution observations of the dense gas tracer HCN, HCO^+, and HNC $J = 1 - 0$ transitions in the Antennae using ALMA. These observations are beam matched and compared to previously obtained lower resolution CO $J = 1 - 0$ observations by Wilson et al. (2000, 2003). We isolate the emission from the nucleus of NGC 4038 and NGC 4039, and from the five SGMCs in the overlap region. We also identify two other bright regions (clouds C6 and C7) located to the north of the overlap region.

1. We compare our interferometric observations of HCN and CO $J = 1 - 0$ with single-dish observations of the same transitions by Gao et al. (2001). We find that ~68% of the total HCN flux from the Gao et al. (2001) observations is located within the nuclei, SGMCs, and clouds C6 and C7, while ~46% of the CO emission is from these same regions. Furthermore, assuming a line ratio of $L_{HCN}/L_{CO} \sim 0.04$, we find that there may be up to 20% of the CO emission that is not associated with any HCN emission. We suggest that this CO is subthermally excited and the emission originates from relatively diffuse molecular gas, similar to that seen in M51.
2. The dense gas fraction as measured by L_{HCN}/L_{CO} is higher in the two nuclei (0.083 and 0.068, respectively) than in any other region of the Antennae (<0.053). Furthermore, the line-ratio peaks in the center of the two nuclei. This increase is consistent with what is seen within the bulges of nearby spiral galaxies, where the stellar potential is larger. We attribute this increase in the dense gas fraction to an increase in the pressure within the two nuclei due to the higher stellar potential in the bulge region.
3. The ratio of L_{HNC}/L_{HCN} is a tracer of mechanical heating within PDRs. We find that this ratio varies by less than a factor of 1.5 across our defined regions in the Antennae, ranging from 0.25 to 0.38. By comparing these values to PDR models that include mechanical heating, we find that mechanical heating must be at least 5% of the PDR surface heating in the Antennae. In these PDR models, a minimum contribution of 10% of mechanical heating relative to PDR surface heating indicates temperatures >100 K, which is consistent with the values we measure. This may indicate that both HCN and HNC $J = 1 - 0$

are tracers of warm, dense molecular gas in the Antennae as opposed to cold, dense molecular gas. A multi-transitional non-LTE excitation analysis would be useful to determine the temperature of this gas.

4. The L_{HCN}/L_{HCO+} ratio peaks in the nucleus of NGC 4038 ($L_{HCN}/L_{HCO+} \sim 1.0$), while it is approximately a factor of two smaller in the overlap region. This difference may be due to a increase in the abundance of HCO^+ in the overlap region due to an increase in the cosmic ray rate from an increased supernova rate. We also find a difference in the ratio between NGC 4038 and NGC 4039 (~0.6). It seems unlikely that this difference is due to an increased supernova rate; a hidden AGN in NGC 4039 could be an additional source of cosmic rays. However, since few studies have shown any evidence of a hidden AGN its existence remains speculative.

We thank the referee for comments that substantially improved the discussion and analysis. This paper makes use of the following ALMA data: ADS/JAO. ALMA#2012.1.00185.S. ALMA is a partnership of ESO (representing its member states), NSF (USA), and NINS (Japan), together with NRC (Canada), NSC and ASIAA (Taiwan), and KASI (Republic of Korea), in cooperation with the Republic of Chile. The Joint ALMA Observatory is operated by ESO, AUI/NRAO, and NAOJ. The National Radio Astronomy Observatory is a facility of the National Science Foundation operated under cooperative agreement by Associated Universities, Inc. The research of C.D.W. is supported by NSERC Canada. This research made use of the python plotting package matplotlib (Hunter 2007). This research made use of APLpy, an open-source plotting package for Python hosted at http://aplpy.github.com.

REFERENCES

Baan, W. A., Henkel, C., Loenen, A. F., Baudry, A., & Wiklind, T. 2008, A&A, 477, 747
Bigiel, F., Leroy, A. K., Blitz, L., et al. 2015, ApJ, 815, 103
Brandl, B. R., Snijders, L., den Brok, M., et al. 2009, ApJ, 699, 1982
Calzetti, D., Wu, S.-Y., Hong, S., et al. 2010, ApJ, 714, 1256
Clements, D. L., Sutherland, W. J., McMahon, R. G., & Saunders, W. 1996, MNRAS, 279, 477
Gao, Y., Lo, K. Y., Lee, S.-W., & Lee, T.-H. 2001, ApJ, 548, 172
Gao, Y., & Solomon, P. M. 2004a, ApJS, 152, 63
Gao, Y., & Solomon, P. M. 2004b, ApJ, 606, 271
García-Burillo, S., Usero, A., Alonso-Herrero, A., et al. 2012, A&A, 539, A8
Graciá-Carpio, J., García-Burillo, S., Planesas, P., & Colina, L. 2006, ApJL, 640, L135
Helfer, T. T., & Blitz, L. 1997a, ApJ, 478, 233
Helfer, T. T., & Blitz, L. 1997b, ApJ, 478, 162
Herrera, C. N., Boulanger, F., Nesvadba, N. P. H., & Falgarone, E. 2012, A&A, 538, L9
Hopkins, P. F., Hernquist, L., Cox, T. J., et al. 2006, ApJS, 163, 1
Hunter, J. D. 2007, CSE, 9, 90
Johnson, K. E., Leroy, A. K., Indebetouw, R., et al. 2015, ApJ, 806, 35
Juneau, S., Narayanan, D. T., Moustakas, J., et al. 2009, ApJ, 707, 1217
Kazandjian, M. V., Meijerink, R., Pelupessy, I., Israel, F. P., & Spaans, M. 2012, A&A, 542, A65
Kazandjian, M. V., Meijerink, R., Pelupessy, I., Israel, F. P., & Spaans, M. 2015, A&A, 574, A127
Klaas, U., Nielbock, M., Haas, M., Krause, O., & Schreiber, J. 2010, A&A, 518, L44
Lintott, C., & Viti, S. 2006, ApJL, 646, L37
Liu, F., & Gao, Y. 2010, ApJ, 713, 524
Loenen, A. F., Baan, W. A., & Spaans, M. 2007, in IAU Symp. 242, Astrophysical Masers and their Environments, ed. J. M. Chapman, & W. A. Baan (Cambridge: Cambridge Univ. Press), 462
Loenen, A. F., Spaans, M., Baan, W. A., & Meijerink, R. 2008, A&A, 488, L5
McCall, B. J., Huneycutt, A. J., Saykally, R. J., et al. 2003, Natur, 422, 500
Meijerink, R., Spaans, M., Loenen, A. F., & van der Werf, P. P. 2011, A&A, 525, A119
Neff, S. G., & Ulvestad, J. S. 2000, AJ, 120, 670
Papadopoulos, P. P. 2007, ApJ, 656, 792
Pety, J., Schinnerer, E., Leroy, A. K., et al. 2013, ApJ, 779, 43
Pierre Auger Collaboration et al. 2007, Sci, 318, 938
Röllig, M., Abel, N. P., Bell, T., et al. 2007, A&A, 467, 187
Rosolowsky, E., & Leroy, A. 2006, PASP, 118, 590
Sakamoto, K., Aalto, S., Evans, A. S., Wiedner, M. C., & Wilner, D. J. 2010, ApJL, 725, L228
Sanders, D. B., & Mirabel, I. F. 1996, ARA&A, 34, 749
Sanders, D. B., Soifer, B. T., Elias, J. H., et al. 1988, ApJ, 325, 74
Schilke, P., Walmsley, C. M., Pineau Des Forets, G., et al. 1992, A&A, 256, 595
Schirm, M. R. P., Wilson, C. D., Parkin, T. J., et al. 2014, ApJ, 781, 101
Schulz, A., Henkel, C., Muders, D., et al. 2007, A&A, 466, 467
Schweizer, F., Burns, C. R., Madore, B. F., et al. 2008, AJ, 136, 1482
Stanford, S. A., Sargent, A. I., Sanders, D. B., & Scoville, N. Z. 1990, ApJ, 349, 492
Steinmetz, M., & Navarro, J. F. 2002, NewA, 7, 155
Talbi, D., Ellinger, Y., & Herbst, E. 1996, A&A, 314, 688
Ueda, J., Iono, D., Petitpas, G., et al. 2012, ApJ, 745, 65
Usero, A., Leroy, A. K., Walter, F., et al. 2015, AJ, 150, 115
Wang, Z., Fazio, G. G., Ashby, M. L. N., et al. 2004, ApJS, 154, 193
Whitmore, B. C., Brogan, C., Chandar, R., et al. 2014, ApJ, 795, 156
Whitmore, B. C., Chandar, R., Schwiezer, F., et al. 2010, AJ, 140, 75
Whitmore, B. C., Zhang, Q., Leitherer, C., et al. 1999, AJ, 118, 1551
Williams, J. P., de Geus, E. J., & Blitz, L. 1994, ApJ, 428, 693
Wilson, C. D., Petitpas, G. R., Iono, D., et al. 2008, ApJS, 178, 189
Wilson, C. D., Scoville, N., Madden, S. C., & Charmandaris, V. 2000, ApJ, 542, 120
Wilson, C. D., Scoville, N., Madden, S. C., & Charmandaris, V. 2003, ApJ, 599, 1049
Wu, H., Cao, C., Hao, C.-N., et al. 2005a, ApJL, 632, L79
Wu, J., Evans, N. J., II, Gao, Y., et al. 2005b, ApJL, 635, L173
Zhang, H.-X., Gao, Y., & Kong, X. 2010, MNRAS, 401, 1839